CCI

BIOMASS

END TO END ECV UNCERTAINTY BUDGET VERSION 3.0

DOCUMENT REF:	CCI_BIOMASS_E3UB_V3
DELIVERABLE REF:	D2.3-E3UB
VERSION:	1.0
CREATION DATE:	2020-06-14
LAST MODIFIED	2020-06-14

Document Authorship

	NAME	FUNCTION	ORGANISATION	SIGNATURE	DATE
PREPARED	M. Santoro		GAMMA		
PREPARED	O. Cartus		GAMMA		
VERIFIED	H. Kay		Aberystwyth University		
VERIFIED	R. Lucas		Aberystwyth University		
PREPARED					
PREPARED					
PREPARED					
PREPARED					
PREPARED					
PREPARED					
VERIFIED	S. Quegan	Science Leader	Sheffield University		
APPROVED					

Document Distribution

ORGANISATION	NAME	QUANTITY
ESA	Frank Seifert	

Document History

VERSION	DATE	DESCRIPTION	APPROVED
1.0	2019-02-27	E3UB of CCI Biomass year 1	
2.0	2020-02-28	E3UB of CCI Biomass year 2	
3.0	2021-06-14	E3UB of CCI Biomass year 3	

Document Change Record (from Year 1 to Year 3)

VERSION	DATE	DESCRIPTION	APPROVED
2.0	2020-02-28	Updated the document to reflect changes in the ATBD of year 2	
3.0	2021-06-14	Updated the document to reflect changes in the ATBD of year 3	

Table of Contents

	Ref	CCI Biomass End to End ECV Uncertainty Budget v3	
esa	Issue	Page	Date
	1.0	4	2021-06-14

biomass cci

LIST OF FIGURES

SYMBOLS AND ACRONYMS

ADP	Algorithm Development Plan
AGB	Above-ground Biomass
ALS	Airborne Laser Scanner
ASAR	Advanced Synthetic Aperture Radar
ATBD	Algorithm Theoretical Basis Document
BCEF	Biomass Conversion & Expansion Factor
BEF	Biomass Expansion Factor
CCI	Climate Change Initiative
CCI-Biomass	Climate Change Initiative – Biomass
DARD	Data Access Requirements Document
DEM	Digital Elevation Model
E3UB	End to End ECV Uncertainty Budget
ECV	Essential Climate Variables
ENL	Equivalent Number of Looks
ENVISAT	ESA Environmental Satellite
EO	Earth Observation
ESA	European Space Agency
FAO	Food and Agriculture Organization
FBD	Fine Beam Dual
GCOS	Global Climate Observing System
GEZ	Global Ecological Zones
GLAS	Geoscience Laser Altimeter System
ICESAT GLAS	Ice, Cloud, and land Elevation Satellite Geoscience Laser Altimeter System
JAXA	Japan Aerospace Exploration Agency
MPI-BGC	Max Planck Institute for Biogeochemistry
PSD	Product Specification Document
PVASR	Product Validation and Algorithm Selection Report
SAR	Synthetic Aperture Radar
URD	User Requirements Document
VCF	Vegetation Continuous Fields

Table 1-1: Reference Documents

ID	Title	Issue	Date
RD-1	Users Requirements Document		
RD-2	Product Specification Document		
RD-3	Data Access Requirements Document		
RD-4	Product Validation and Algorithm Selection		
RD-5	Algorithm Theoretical Basis Document		
RD-6	Algorithm Development Plan		
RD-7	Product Validation Plan		
RD-8	Algorithm Theoretical Basis Document of GlobBiomass project		

1 Introduction

Above-ground biomass (AGB, units: Mg ha^{-1}) is defined by the Global Carbon Observing System (GCOS) as one of more than 50 Essential Climate Variables (ECV). For climate science communities, AGB is a pivotal variable of the Earth System, as it impacts the surface energy budget, the land surface water balance, the atmospheric concentration of greenhouse gases and a range of ecosystem services. The GCOS requirement is for AGB to be provided wall-to-wall over the entire globe for all major woody biomes at 500 m to 1 km spatial resolution with a relative error of less than 20% where AGB exceeds 50 Mg ha^{-1} and a fixed error of 10 Mg ha^{-1} where the AGB is below that limit.

One of the objectives of the CCI Biomass project is to generate global maps of AGB using a variety of Earth Observation (EO) datasets using state-of-the-art models for three epochs (2010, 2017 and 2018) and assess biomass changes on both a yearly time scale and an almost decadal time scale. The maps should be spatially and temporally consistent; in addition, they need to be consistent with other data layers thematically similar to the AGB dataset produced in the framework of the CCI Programme (e.g., Fire, Land Cover, Snow etc.).

Algorithms to estimate AGB and its changes are described in the Algorithm Theoretical Basis Document (ATBD) [RD-5]. The scope of this document is to define and quantify the uncertainties associated with the biomass estimates. This End to End ECV Uncertainty Budget document (E3UB) relies on indications in the User Requirements Document (URD) [RD-1], the Product Specifications Document (PSD) [RD-2] and the Data Access Requirements Document (DARD) [RD-3]. Advances, such as those described in the Product Validation and Algorithm Selection Report (PVASR) [RD-4], that may potentially be implemented in future revisions of the ATBD and in this document are described in the Algorithm Development Plan (ADP) [RD-6].

During Year 1 of the project, methods were developed that led to the generation of the global AGB product for the year 2017. In year 2, the methods were refined to generate a set of three global datasets of AGB for the years 2010, 2017 and 2018. In year 3, the AGB estimation methods have been refined towards an improved set of AGB maps, also allowing for an assessment of AGB changes between epochs. Accordingly, with each iteration, the framework that quantifies the uncertainties of each map has been set and updated. This report documents the framework adopted to quantify the precision of the AGB and AGB change estimates.

Section 2 provides the background of this E3UB, describing the strategy that underpins the algorithms implemented in CCI Biomass to estimate AGB and AGB change. Sections 3 and 4 describe the procedures implemented to characterize the precision of the AGB and the AGB change estimates, respectively.

2 Background

Accuracy describes how well the estimate of a certain quantity (e.g., AGB) matches its true value. For an ensemble of data, two gross statistical measures of the precision of the estimator are commonly used: bias, which is the expected value of the difference between the estimated and true value, and a quantity indicating the variability of the estimate (standard deviation). More complete descriptors could include, for example, confidence intervals on the estimates or the full error distribution. These descriptors are, however, practically impossible to obtain in our case because the errors of some of the parameters involved in the biomass retrieval scheme could only be assumed. A framework to estimate the bias of an AGB estimate is introduced in the ATBD of this project. The focus of this document is the characterization of the precision of the AGB and AGB change estimates starting from the standard deviation of the observations and the model parameters.

In the case of AGB retrieval, the precision of the retrieved value depends on the precision of the input data and the precision of the estimation procedure. Figure 2-1 shows the flowchart of the CORE AGB estimation procedures implemented in year 1 and then in successive years of the CCI Biomass project to generate global datasets of AGB estimates for the three epochs envisaged by CCI Biomass [RD-5].
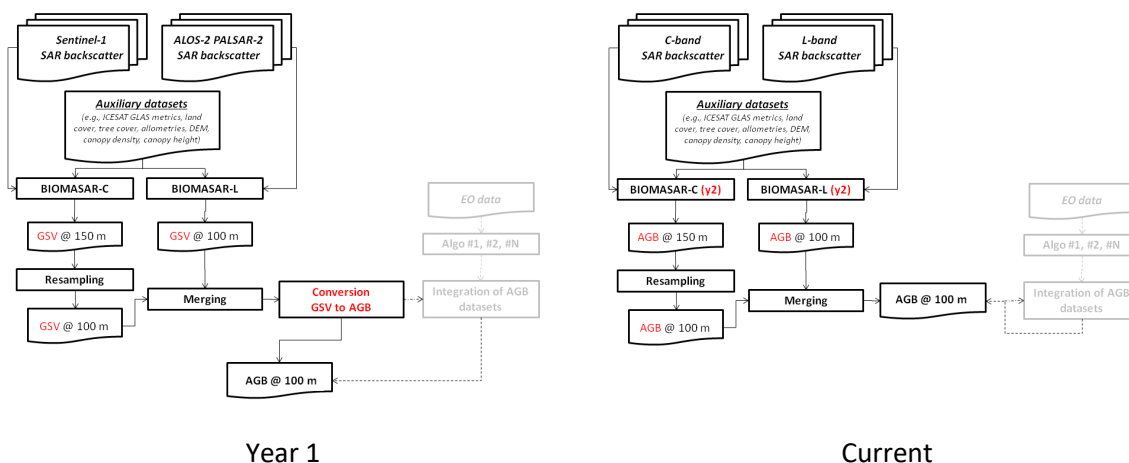
Year 1   Current

Figure 2-1: Functional dependencies of datasets and approaches forming the CCI Biomass CORE global biomass retrieval algorithm (right) and for year 1 (left). Text in red visualizes modifications introduced from year 1 to year 2, i.e., the current version of the CORE algorithm. The shaded part of the flowchart represents potential improvements following the implementation of additional retrieval techniques [RD-5].

The CORE algorithm implemented in year 1 foresees that two independent estimates of growing stock volume (GSV, unit: m^3 ha^{-1}) are obtained from the BIOMASAR algorithm adapted to ingest C-band (BIOMASAR-C) and L-band data (BIOMASAR-L). The estimates are combined to obtain a final estimate that should be characterized by smaller errors than the original values. Since the C- and L-band datasets have different pixel spacing, the GSV estimates from the BIOMASAR-C algorithm have slightly

lower resolution so are resampled to the geometry of the BIOMASAR-L estimates. Finally, GSV is converted to AGB with a Biomass Conversion and Expansion Factor (BCEF).

Starting with year 2, the retrieval strategy has not changed but we have modified the inversion models by expressing them directly as a function of AGB. The Water Cloud Model now foresees that the SAR backscatter is related to canopy density and height. Allometries linking these two variables as well as canopy height to AGB allow AGB to be directly included in the Water Cloud Model without having to rely on empirical coefficients, as is usually done.

The quantification of the standard deviation of an AGB estimate is described in Section 3 for each of the implementations, following the description of the algorithms in the ATBD.

AGB changes can be estimated either by differencing signals or by differencing estimates of AGB. The latter approach propagates errors of individual estimates but is the only viable solution if the framework to estimate changes considers multiple predictors, which furthermore have different characteristics (e.g., density of observations). The synergy of spaceborne observations being the major strength of the CORE algorithm to obtain a reliable distribution of AGB estimates worldwide, the AGB change products developed in this context rely on the individual maps rather than on the EO observations. The AGB change products are defined simply as the difference between maps between two epochs; here, we describe the quantification of the uncertainties, following the description of the AGB change product in the ATBD.

3 Methods to assign precision to AGB estimates

In this Section, we detail methods to quantify the standard deviation for each of the individual global inversion methods and for the final AGB product. First, we summarize the current two implementations of the CCI Biomass CORE algorithm (Section 3.1). Then, the precision of the estimates from BIOMASAR-C and BIOMASAR-L are presented (Sections 3.2 and 3.3, respectively). The methods presented reflect our current understanding of the standard deviations embedded in the retrieval algorithms.

3.1 The modelling framework

The Water Cloud Model (WCM) with gaps, given as Equation (3-1), was derived from the original WCM presented by (Attema & Ulaby, 1978) to express the total forest backscatter of a forest as the sum of direct scattering from the ground through gaps in the canopy, ground scattering attenuated by the canopy and direct scattering from vegetation:

$$\sigma^0_{for} = (1 - \eta)\sigma^0_{gr} + \eta\sigma^0_{gr}T_{tree} + \eta\sigma^0_{veg}(1 - T_{tree}) \tag{3-1}$$

Here η is the area-fill or canopy density factor, representing the fraction of the area covered by vegetation, σ^0_{gr} and σ^0_{veg} represent the backscattering coefficients of the ground and vegetation layer, respectively, and T_{tree} is the two-way tree transmissivity, which can be expressed as $e^{-\alpha h}$, where α is the two-way attenuation per meter through the tree canopy and h is the depth of the attenuating layer.

Another formulation of the WCM relates the forest backscatter directly to the GSV:

$$\sigma^0_{for} = \sigma^0_{gr}e^{-\beta V} + \sigma^0_{veg}\left(1 - e^{-\beta V}\right) \tag{3-2}$$

where β is an empirically defined coefficient expressed in ha m^{-3} and expresses the forest transmissivity modelled as a simple exponential of the GSV, *V*.

By comparing Equations (3-1) and (3-2), the link between β, η and α is given by (Santoro et al., 2002):

$$e^{-\beta V} = 1 - \eta\left(1 - e^{-\alpha h}\right) \tag{3-3}$$

While Equation (3-3) can be considered valid in mature forests because height and GSV (or AGB) are almost linearly related, it is not correct throughout the entire range of biomass because of the non-linear relationship between the forest variables: height, biomass, volume and canopy density.

Equation (3-2) was used in year 1 of CCI Biomass to estimate GSV. Starting with year 2, we considered the original WCM with gaps in Equation (3-1) and the set of functional dependencies between canopy density, tree height and above-ground biomass to express the WCM as a function of AGB [RD-5].

$$CD = 1 - e^{-qh} \tag{3-4}$$

$$AGB = p_1 H^{p_2} \tag{3-5}$$

The empirical coefficients *q*, p_1 and p_2 are regression coefficients estimated by means of non-linear least squares [RD-5]. The estimation of the parameter *q* was supported by canopy density (CD) and height (h) derived from ICESat GLAS measurements of canopy density and top-of-canopy height (RH100). The estimation of the parameters p_1 and p_2 was supported by the RH100 ICESat GLAS measurements and corresponding surrogate AGB values from the GlobBiomass dataset of 2010 (Santoro et al., 2020). The justification for using map values instead of in situ measurements of AGB has been outlined in the ATBD [RD-5].

In the following sections, we provide a description of the errors in each of the two retrieval methods.

3.1.1 BIOMASAR for GSV retrieval

The parameters σ^0_{gr} and σ^0_{veg} are unknown a priori and need to be estimated. The estimate of σ^0_{gr} corresponds to the mean value of the SAR backscatter for pixels characterized by low canopy cover (so-called "ground" pixels) around the pixel of interest. The estimate of σ^0_{veg} is obtained from the mean value of the SAR backscatter for pixels characterized by high canopy cover (so-called "dense forest" pixels) around the pixel of interest. This value, referred to as σ^0_{df}, is compensated for the residual ground contribution due to the canopy not being completely opaque. The estimation of σ^0_{veg} from σ^0_{df} and σ^0_{gr} is done in slightly different ways depending on whether GSV is estimated from C-band SAR (BIOMASAR-C) or L-band SAR backscatter data (BIOMASAR-L) [RD-5]. In addition, an estimate of the coefficient of the two-way forest transmissivity, β, is needed, together with an estimate of the GSV of dense forest (V_{df}, BIOMASAR-C) or canopy height and canopy density of dense forests (h_{df} and η_{df}, BIOMASAR-L) [RD-5].

Once the model parameters have been estimated, the inversion of the WCM in Equation (3-2) is straightforward.

$$\hat{V} = -\frac{1}{\beta} ln\left(\frac{\sigma^0_{meas} - \sigma^0_{veg}}{\sigma^0_{gr} - \sigma^0_{veg}}\right) \tag{3-6}$$

Given N observations of the SAR backscatter acquired at different times, the corresponding N estimates of GSV can be combined with a weighted average to form a new estimate of GSV. The resulting estimate will have higher precision than any of the individual GSV estimates but may not be closer to the true GSV if the estimates are biased.

$$V_{mt} = \frac{\sum_{i=1}^{N} w_i \widehat{V}_i}{\sum_{i=1}^{N} w_i} \tag{3-7}$$

The weights, w_i, in Equation (3-7) are defined as the vegetation-to-ground backscatter difference in dB, $\sigma^0_{veg} - \sigma^0_{gr}$, normalized by the maximum backscatter difference:

$$w_i = \frac{\sigma^0_{veg,i} - \sigma^0_{gr,i}}{max(\sigma^0_{veg,i} - \sigma^0_{gr,i})} \tag{3-8}$$

Merging of the BIOMASAR-C and BIOMASAR-L estimates of GSV is implemented in the form of a weighted average, where the weights account for three different calculated weights combined into one [RD-5]:

$$GSV = w(L)V_{mt,L} + w(C)V_{mt,C} \tag{3-9}$$

Estimation of AGB is a simple scaling of GSV with the BCEF.

$$AGB = BCEF \cdot GSV \tag{3-10}$$

where BCEF is the product of wood density (g/cm^3) and the total-to-stem biomass ratio.

3.1.2 BIOMASAR for AGB retrieval

The parameters σ^0_{gr}, σ^0_{veg} and α are unknown a priori and need to be estimated.

For BIOMASAR-C, it is assumed that α remains constant and its uncertainty can be neglected because of its minimal impact on the retrieval. The estimates of σ^0_{gr} and σ^0_{veg} are obtained with a least squares regression of Equation (3-11), i.e., a simplified version of the original WCM assuming that the tree transmissivity component is negligible [RD-5]. The tree cover dataset is used as reference for the parameter η. The procedure is applied separately to each set of backscatter measurements and percent tree cover values characterized by a specific range of incidence angles.

$$\sigma^0_{for} = (1 - \eta)\sigma^0_{gr} + \eta\sigma^0_{veg} \tag{3-11}$$

For BIOMASAR-L, all three parameters need to be estimated. Equation (3-1) is therefore regressed to observations of canopy density and SAR backscatter, using the allometry in Equation (3-4) to replace height with canopy density (η) [RD-5]. The procedure is applied separately to each set of backscatter measurements and percent tree cover values characterized by a specific range of incidence angles.

Once the allometries (3-9) and (3-10) have been inserted into Equation (3-1), the inversion of the WCM to estimate AGB is done numerically. Having multiple observations of the backscatter at C-band implies that the final estimate of AGB is obtained with the same procedure as is described in Section 3.1.1, Equations (3-7) and (3-8).

3.2 Quantifying the precision of the BIOMASAR-C estimates

3.2.1 Accuracy of the C-band backscatter measurements

The precision of a backscatter measurement is affected by the radiometric and calibration accuracies, thermal noise and speckle. The SAR pre-processing also introduces additional uncertainty related to: (i) the precision of the geocoding transformation and resampling between radar and map geometries; (ii) the horizontal and vertical precision of the Digital Elevation Model (DEM) used as reference for the map geometry, and (iii) the precision of the pixel area and local incidence angle used to normalize the backscatter for slope-induced effects on the backscatter. Since the pixel-level uncertainties in the DEMs used in this study are unavailable, we cannot estimate the variance of a backscatter measurement from the individual variances of the terms listed above. We therefore estimate it empirically by equating it to the Equivalent Number of Looks (ENL).

In the ATBD [RD-5], our estimate of the ENL for Sentinel-1 was 162 (median value) with a span of [90, 375] but most values lie between 100 and 250. Assuming a constant ENL of 162 for Sentinel-1, we obtain a standard deviation of 0.32 dB. In Santoro et al. (2015), we quantified the standard deviation of Envisat ASAR backscatter observations as a function of the number of observations available in the multi-channel speckle filter: 0.6 dB for N ≤ 50; 0.5 dB for 51 ≤ N ≤ 150; and 0.4 dB for N > 150, where N is the number of backscatter observations at a pixel.

These values are here used to characterize the $\delta\sigma^0_{meas}$ component of the standard deviation of the biomass estimates (see Equation (3-12)).

3.2.2 BIOMASAR for GSV retrieval

The precision of a biomass estimate obtained from a single observation of the SAR backscatter is quantified by propagating the standard deviation of (i) the measured SAR backscatter, σ^0_{meas}, and (ii) the estimates of the forest backscatter model parameters σ^0_{gr}, σ^0_{df}, β and V_{df}. Since the standard deviations of the five random variables listed above are uncorrelated and small (see below), the standard deviation of the estimate of GSV obtained from a single backscatter observation, δV, is given by:

$$\delta V = \sqrt{\begin{array}{c} (\delta\sigma^0_{meas})^2 \cdot \left(\frac{\partial V}{\partial\sigma^0_{meas}}\right)^2 + \left(\delta\sigma^0_{gr}\right)^2 \cdot \left(\frac{\partial V}{\partial\sigma^0_{gr}}\right)^2 + \left(\delta\sigma^0_{df}\right)^2 \cdot \left(\frac{\partial V}{\partial\sigma^0_{df}}\right)^2 + \\ + (\delta\beta)^2 \cdot \left(\frac{\partial V}{\partial\beta}\right)^2 + \left(\delta V_{df}\right)^2 \cdot \left(\frac{\partial V}{\partial V_{df}}\right)^2 \end{array}}$$

(3-12)

Each of the partial derivatives in Equation (3-12) is derived from Equation (3-3) (Annex A).

The standard deviation of the model parameters expressing the backscatter from the ground, $\delta\sigma^0_{gr}$, and dense forest, $\delta\sigma^0_{df}$, combines the standard deviation in the observations of the pixels labelled as unvegetated or dense forest, respectively, and the standard deviation of the backscatter for the tree cover values representing the "ground" and "dense forest" classes. Here σ^0_{gr} and σ^0_{df} are estimated from the histograms of the SAR backscatter measurements for unvegetated and dense forest pixels (see Figure 9 in Santoro et al., 2011). In summary, the standard deviations $\delta\sigma^0_{gr}$ and $\delta\sigma^0_{df}$ are obtained

by subtracting the variance associated with the backscatter measurements, i.e., $\delta\sigma_{meas}^{0}{}^{2}$, from the variance of the histogram for "ground" pixels and "dense forest" pixels, respectively.

The estimates of the coefficient β and the corresponding standard deviation $\delta\beta$ are defined in the ATBD of the GlobBiomass project (available at http://globbiomass.org/products/global-mapping/) [RD-8]. For each ecological zone of the FAO Global Ecological Zones (GEZ) dataset (see [RD-5] for details), the coefficient β was set equal to the value of the exponential model relating MODIS Vegetation Continuous Fields (VCF) estimates of canopy cover and GSV from map datasets. Accordingly, the standard deviation was defined as the mean standard deviation of the observations. It is important to remark that this is an educated guess due to the lack of observations of forest transmissivity from different biomes.

The standard deviation of the V_{df} parameter, δV_{df}, was also discussed in the ATBD of the GlobBiomass project [RD-8]. A global raster was obtained with RandomForest (Breiman, 2001) models for each ecoregion of the FAO GEZ dataset using a set of initial estimates of V_{df} from various sources [RD-5] as response and the WorldClim [RD-5] and ICESAT GLAS layers of forest height and density [RD-5] as predictors. Figure 3-1 illustrates the predictive performance of the models for each FAO ecoregion with the comparison of Out-Of-Bag model predictions (i.e., bootstrap aggregation of predictions from 500 regression tree models) versus the initial estimates for V_{df} from the reference database. These values suggest that the standard deviation associated with RandomForest predictions for V_{df} is of the order of 15 to 60% with the largest error of 40 to 60% for sub-tropical and tropical dry forests. This approximation might be too coarse but is currently our best achievable estimate.
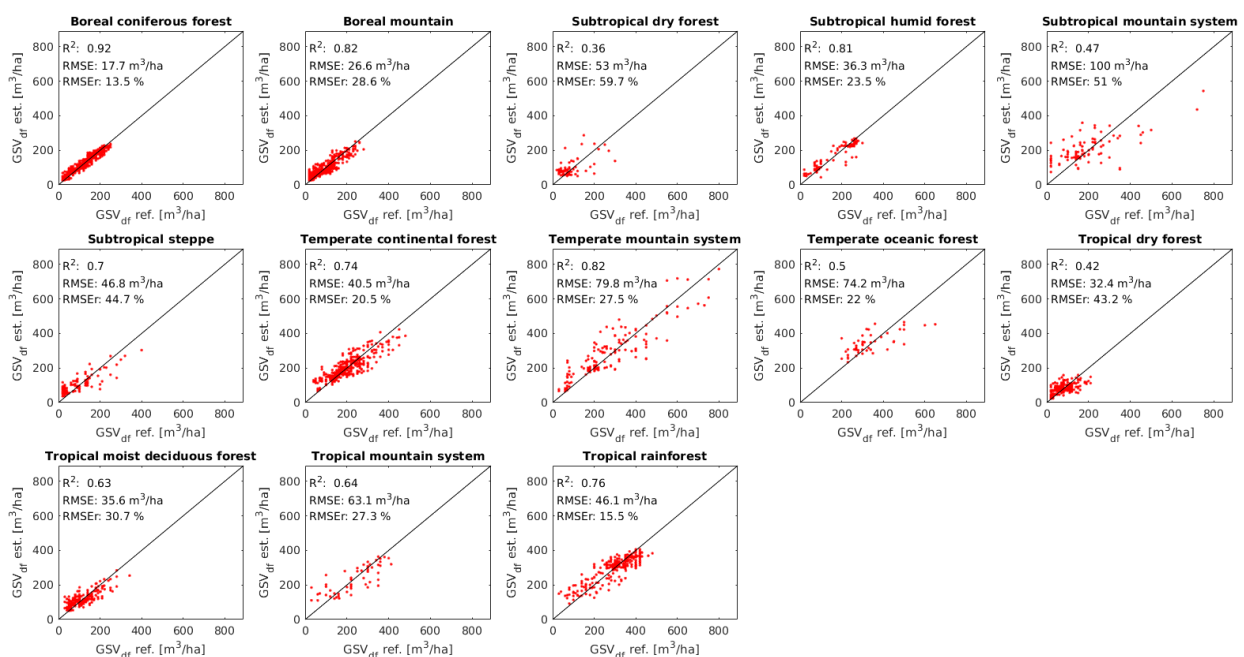
Figure 3-1: RandomForest predictions of the GSV of dense forests per 2°x2° grid cell derived from WorldClim and ICESAT GLAS versus estimates derived from inventory, provincial/state reports or existing maps.

The multi-temporal GSV estimate is obtained as a linear combination of GSV estimates from images acquired at different times. The aim of the multi-temporal combination is to reduce noise affecting each single estimate of GSV. Accordingly, the standard deviation of the multi-temporal estimate of

GSV is obtained as the square root of the sum of the variances weighted with the coefficients w_i in Equation (3-8).

If the backscatter observations were independent of each other, the standard deviation of the final GSV estimate would correspond to the weighted sum of the standard deviations of each individual GSV estimate. In reality, observations are correlated, so the standard deviation of the multi-temporal GSV estimates is the sum of a variance component and a covariance component that accounts for the correlation between errors.

$$\delta(V_{mt})^2 = \sum_{i=1}^{N} w_i^2 \, \delta(V_i)^2 + 2 \sum_{i=1}^{N-1} \sum_{j=i+1}^{N} w_i \, w_j \, Cov(V_i, V_j) \qquad (3\text{-}13)$$

where

$$Cov(V_i, V_j) = \delta V_i \delta V_j r_{ij} \qquad (3\text{-}14)$$

The variance component of the standard deviation of the multi-temporal GSV estimate is modelled as a linear combination of the single-image GSV variances given by Equation (3-3). Here, it is assumed that the multi-temporal weights are the best estimates of the individual variances of the individual estimates of GSV.

The covariance component is then expressed in a similar manner where individual error co-variances are weighted. The symbol r_{ij} represents the correlation of errors between the estimates of GSV from image i and image j. Such correlation has been neglected in previous studies due to the weak correlation between observations at coarse spatial resolution. Envisat ASAR observations with a pixel size of 1,000 m repeat from the same orbit every 35 days; observations adjacent in time were taken from adjacent orbits and/or different nodes. From this weak correlation, it was assumed that also the correlation of the errors was small. In the case of Sentinel-1, this assumption has been revisited for two reasons. The higher spatial resolution compared to the Envisat ASAR dataset (100 m vs. 1,000 m) allows a more detailed spatial characterization of the biomass. In addition, the constellation formed by the Sentinel-1A and -1B units observes any point on the ground with the same viewing geometry every 6 days; this increases to 12 days for a single satellite. This increases the probability of correlation between retrieval errors.

Computing the correlation of errors requires a reference dataset. The only viable solution is to use maps of AGB, since plot measurements are typically too sparse to allow a spatially explicit characterization of the error covariance. Laser-based maps of AGB are probably the most suitable reference dataset for characterizing the error covariance. Although such maps are not free from errors, it is reasonable to assume that their impact on the correlation of errors is minimal because of their usual high precision. Obviously, maps lacking complete characterization of errors and with low precision should be discarded, which poses a serious issue when attempting to generate wall-to-wall values of the error covariance. This is discussed later in this Section.

Figure 3-2 shows a matrix reporting at each bin the correlation of the errors between Sentinel-1 images i and j using as a reference the GSV predicted from country-wide laser scanning of Sweden (Nilsson et al., 2017). The index on each axis represents the date of acquisition in 2017 (i.e., 1, 2, 3 etc. mean first, second, third, etc.) image acquired in 2017. The correlations have been computed for all pixels within a 1° x 1° grid cell in North Sweden. The impact of the area selected to compute the error correlation is negligible. In Figure 3-2, we observe higher correlations towards the top-left and bottom-right corners, which represent data acquired during the first 3 months of the year (image index between 1 and 180)

and the last 2 months of the year (image index 700 to 814; i.e., under winter/frozen conditions). Similarly, somewhat high correlations can be seen at the top-right and bottom-left corner of the matrix, corresponding to combinations involving an image acquired at the beginning and end of 2017, with both characterized by winter/frozen conditions. Occasionally, high correlation is observed for some of the winter-summer pairs, whereas pairs formed by images acquired under unfrozen conditions were mostly characterized by lower correlation.
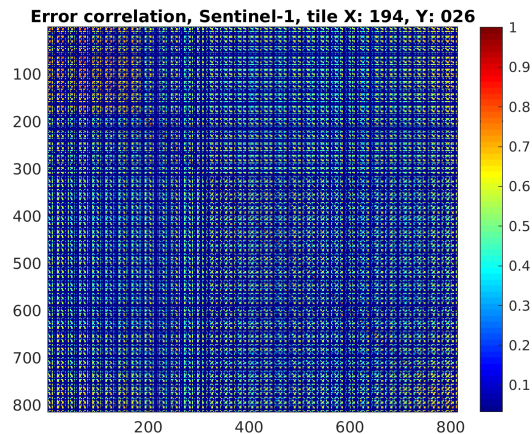

Figure 3-2: Matrix of error correlations for Sentinel-1 GSV estimates for a 1° x 1° area in northern Sweden (Lat: 63°-64°N; Lon: 14°-15°E, corresponding to tile X: 194 and Y: 026)

The histogram of correlations shows the distribution of the error correlation for all combinations of images acquired over the area visualized in Figure 3-3. The mean correlation coefficient was 0.53 with a span of 0.16 to 0.82.
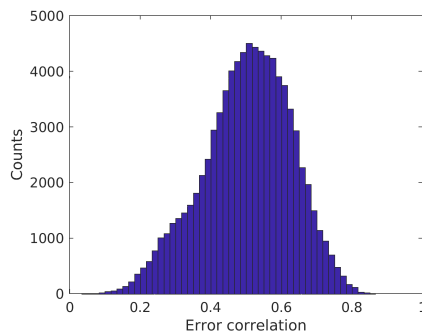

Figure 3-3: Histogram of error correlation for the dataset illustrated in Figure 3-2.

Since the computation of the error correlation requires a reference dataset, the question is whether a model or some general rules can be identified to characterize the correlation, given that no such dataset is available globally. Figure 3-4 and Figure 3-5 show two examples of correlation of errors between a given image and all other images for the 1° x 1° tile considered in Figure 3-2. Figure 3-4 is based on an image acquired under winter/frozen conditions and shows a slight seasonal trend of higher correlation when the other image was also acquired during winter. Figure 3-5 is instead based on an image acquired under summer/unfrozen conditions and shows fairly constant behaviour. These results indicate that a model expressing correlation as a function of time (e.g., exponential decay) does not apply. A model that replicates seasonality would be more suitable but difficult to implement as it

changes in space depending on local climatic conditions. Hence, in the first instance, one could consider using a simple generic value, such as the median of all correlations.
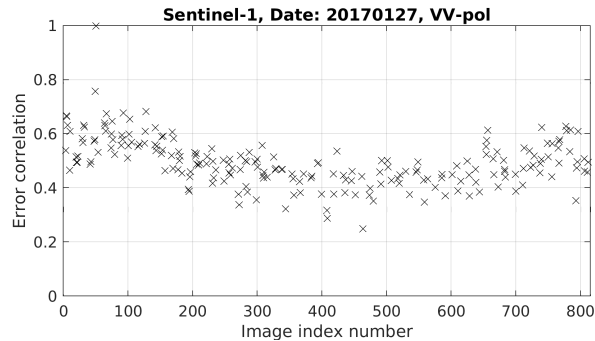

Figure 3-4: Error correlation between GSV estimated from a Sentinel-1 image acquired on 20170127 and all other Sentinel-1 images covering the 1° x 1° tile introduced in Figure 3-2.
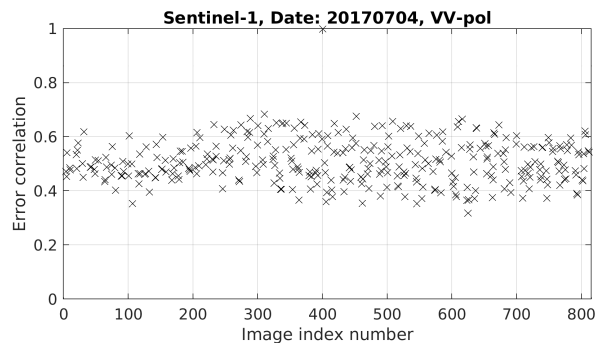

Figure 3-5: Error correlation between GSV estimated from a Sentinel-1 image acquired on 20170704 and all other Sentinel-1 images covering the 1° x 1° tile introduced in Figure 3-2.

The total standard deviation and its components are illustrated in Figure 3-6 for the 1° x 1° tile in North Sweden (lower panels). We also include the map of GSV retrieved with the BIOMASAR-C algorithm and an image showing the number of Sentinel-1 backscatter observations used to retrieve GSV (upper panels). It is notable that, at this stage, GSV has been retrieved regardless of the land cover (i.e., values of GSV have also been associated with water bodies and cropland). These areas need to be masked out for any further analysis of the data. Because of the very large number of observations used to retrieve GSV, the variance term in Equation (3-13) becomes small. The covariance term in Equation (3-13) instead is large because of the large number of combinations, in particular when the temporal correlation between errors remains moderate or high .

The same analysis was repeated for other areas where laser-based maps of AGB are available so as to reinforce the findings obtained in a boreal environment. The results did not differ essentially from those obtained in Sweden. For this reason, we have computed the GSV standard deviation by assuming a constant error correlation, equal to the mean of the correlations shown in the histogram of Figure 3-3. The result is identical to the bottom-right panel in Figure 3-6 showing the covariance term of the standard deviation, suggesting that this simplifying assumption may be introduced to give a global characterization of the error covariance term.
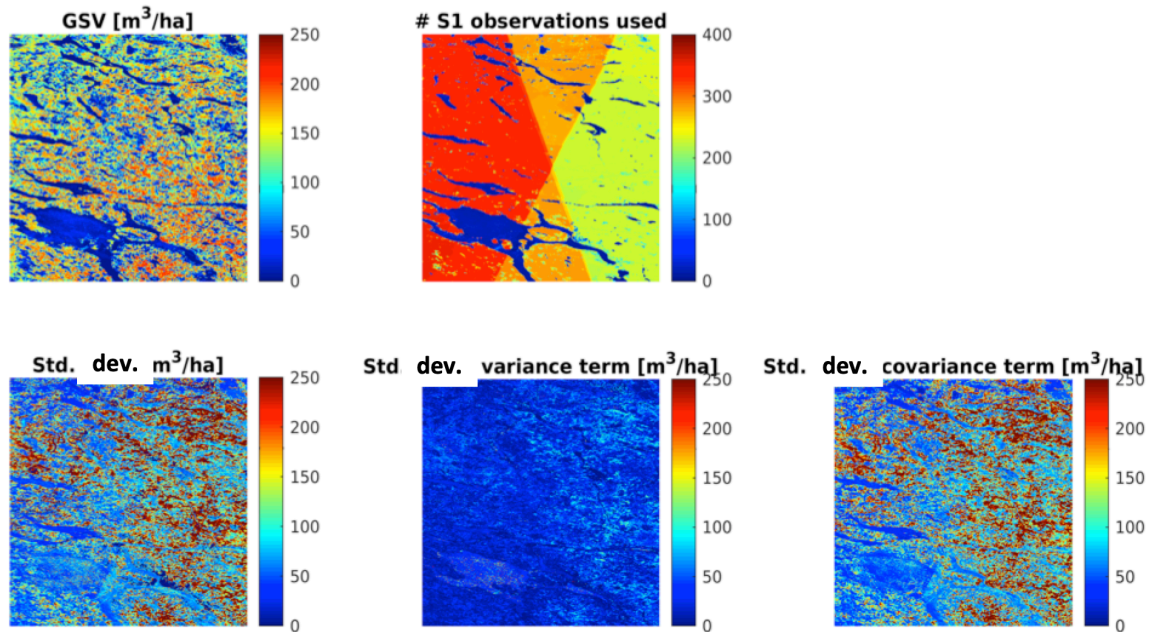
Figure 3-6: Comparing total standard deviations using the correlation matrix shown in Figure 3-2 (left) and a constant correlation matrix with correlation equal to the mean of the error correlation in Figure 3-3.

3.2.3 BIOMASAR for AGB retrieval

The precision of an AGB estimate obtained from a single observation of the SAR backscatter is quantified by propagating the standard deviation of (i) the measured SAR backscatter, σ^0_{meas}, (ii) the estimates of the forest backscatter model parameters σ^0_{gr} and σ^0_{veg}, (iii) the coefficient of the allometric function relating canopy density and RH100, q, and (iv) the coefficients of the allometry relating canopy height and AGB, p_1 and p_2.

The estimates of σ^0_{gr} and σ^0_{veg} are first obtained by least squares regression to the model in Equation (3-11) per 10° wide intervals of local incidence angle; then, a quadratic function is established to describe the variation of each parameter as a function of incidence angle [RD-5]. Accordingly, the standard deviations of σ^0_{gr} and σ^0_{veg} were obtained from the variance-covariance matrix for the fitted coefficients using Equation (3-11). The covariance term was usually much smaller than the variance terms, thus confirming the assumption of the two parameters being independent from each other. Then, the standard deviations of σ^0_{gr} and σ^0_{veg} per incidence angle range are transformed with the error model of the quadratic function to obtain a value for each per incidence angle. The error propagation is programmed in the polyconf tool of the Matlab scripting language.

The standard error of the coefficient q was calculated through bootstrapping with replacement for each of the ecoregions, with 100 iterations per ecoregion. Figure 3-7 shows the spatially explicit map of the standard error of q obtained by interpolating the individual value per ecoregion with bicubic interpolation to avoid offsets at the boundary of ecoregions. The standard error ranged from 0 to 143%, although it was highly correlated with the number of available footprints per ecoregion (Figure 3-8), with ecoregions with more than 100 footprints all having a standard error < 10%. Larger errors were obtain for ecoregions characterized by sparse to almost absent forest cover, in which case the number of GLAS footprints used to estimate q was small.

	Ref	CCI Biomass End to End ECV Uncertainty Budget v3	
esa	Issue	Page	Date
	1.0	17	2021-06-14

biomass cci
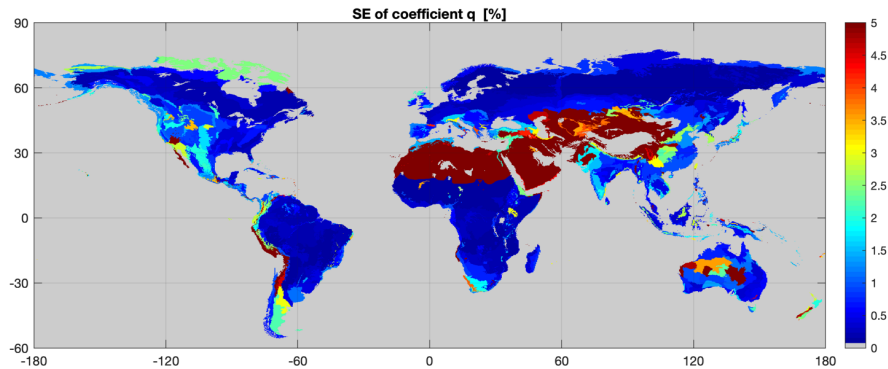
Figure 3-7: Spatially interpolated maps of the standard error of the coefficient q. The map shows the standard error relative to the estimate of each parameter.
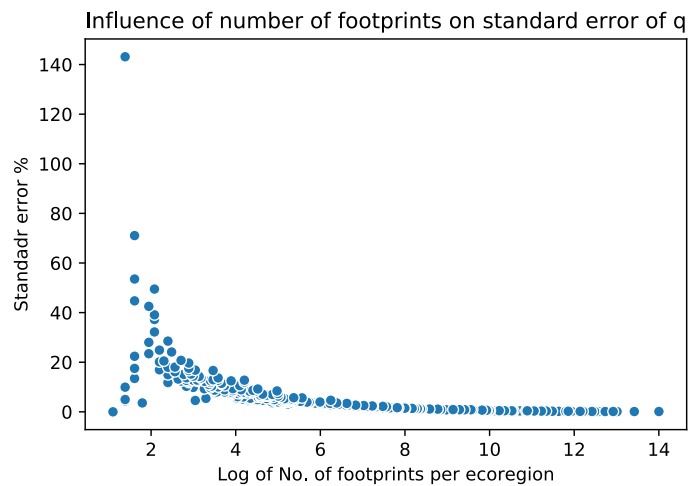
Figure 3-8: Scatterplot demonstrating the influence of the number of available ICESat GLAS footprints within an ecoregion on the standard error of the q value obtained

The standard deviation of the coefficients p_1 and p_2 was obtained from the confidence intervals estimated when fitting AGB from the GlobBiomass dataset and RH100 measurements from the spaceborne LiDAR datasets [RD-5]. Figure 3-9 shows that the standard deviation was mostly below 10% and 5% of the estimated value for p_1 and p_2, respectively, except in regions of sparse forest cover and barren ground. Here, the uncertainty was larger due to the difficulty to fit the allometry to a very small range of AGB and height measurements.

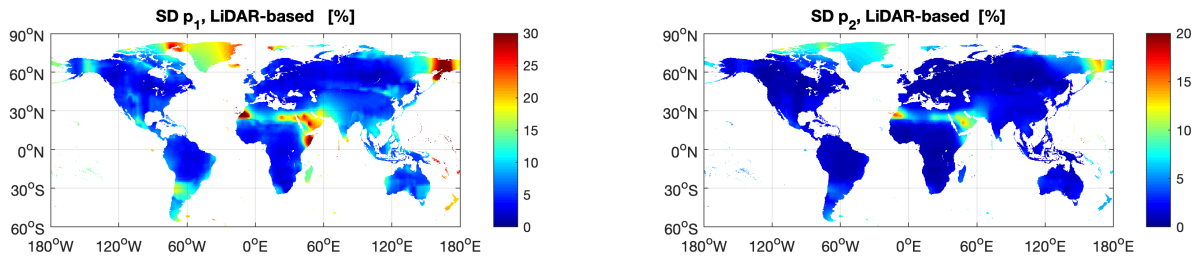Figure 3-9: Spatially interpolated maps of the standard deviation of coefficients p_1 and p_2. The maps show the ratio between the standard deviation and the estimate of each parameter

Because of the numerical inversion to estimate AGB from a backscatter observation, the computation of the standard deviation of an AGB estimate also needs to be handled with a numerical approach. A numerical approach means that the retrieval model parameters involved in the estimation of the AGB (σ^0_{meas}, σ^0_{gr}, σ^0_{veg}, q, p_1 and p_2) are perturbed on the basis of the individual standard deviations and a perturbed AGB is estimated. This procedure is repeated N times for each pixel and in each SAR image so to create for each time a vector of perturbed AGB estimates from which the standard deviation corresponding to a retrieved AGB at a given pixel and image is computed.

As in the case of a retrieval of GSV, the standard deviation of the multi-temporal estimate of AGB is the sum of a variance component and a covariance component that accounts for the correlation between errors.

$$\delta(AGB_{mt})^2 = \sum_{i=1}^{N} w_i^2 \, \delta(AGB_i)^2 + 2 \sum_{i=1}^{N-1} \sum_{j=i+1}^{N} w_i \, w_j \, Cov(AGB_i, AGB_j) \qquad (3\text{-}15)$$

where

$$Cov(AGB_i, AGB_j) = \delta AGB_i \delta AGB_j r_{ij} \qquad (3\text{-}16)$$

The variance component of the standard deviation of the multi-temporal AGB estimate is modelled as a linear combination of the single-image AGB variances. For the covariance term, we assume that the approach developed for the GSV holds true because of the simple scaling between GSV and AGB.

3.3 Quantifying the precision of the BIOMASAR-L estimates

3.3.1 Accuracy of the L-band backscatter measurements

The ALOS-2 FBD and ScanSAR datasets, which were provided by JAXA in the form of global mosaics on an annual basis (FBD) or as per-cycle mosaics (ScanSAR), introduce errors in the AGB retrieval associated with speckle, thermal noise, and errors in calibration, geocoding and topographic corrections.

In the ATBD [RD-5], we documented radiometric and geometric errors that were presumed due to the fact that the SRTM DEM had not been compensated for elevation offsets between the geoid (SRTM reports geoid referenced heights) and the WGS84 ellipsoid. This resulted in systematic geolocation errors of the ALOS-2 backscatter imagery up to several pixels dependent on the Geoid-WGS84 elevation offset. The geolocation error was reduced by means of co-registration of the imagery with a global Landsat NDVI dataset. While the co-registration allowed linear offsets to be corrected, topography-related geolocation errors and also the sub-optimal performance of topogaphic

corrections could not be corrected. Because these errors cannot be quantified at pixel level, we here can only quantify the error associated with speckle.

In order to reduce the speckle in the original ALOS-2 imagery with 25m pixel size, all images were:

1) aggregated to the target pixel size of 100 m (0.00088888°) for the mapping of biomass
2) filtered with the multi-temporal filter suggested in Quegan & Yu (2001).

The ENL of the imagery after filtering was assessed for a number of homogenous forest patches, identified by means of visual image interpretation. Since the performance of the multi-temporal filtering depends on the number of images considered in the filtering as well as the level of speckle correlation between images (which given the repeat intervals of ALOS-2 of 14 days should be low), no global ENL can be specified. In areas where only FBD mosaics were available, we found the ENL to be of the order of 70 to 80. In areas where FBD and ScanSAR imagery could be combined, the ENL was on average of the order of 300.

3.3.2 BIOMASAR for GSV retrieval

The BIOMASAR-C error model used to quantify the standard deviation of a GSV estimate, δV, from a backscatter observation is also applied in the case of BIOMASAR-L. However, some modifications are required because of the differences in the estimation of the parameter σ^0_{veg}.

In the model inverted for GSV, σ^0_{veg} is expressed as a function of the average backscatter observed over dense forests, σ^0_{df}, the average canopy density of dense forests, η_{df}, the average height of dense forests, h_{df}, and the two-way attenuation coefficient, α [RD-5]. The error model therefore needs to be reformulated to consider the error associated with η_{df}, α, and h_{df}:

$$\delta V = \sqrt{\begin{array}{l}(\delta\sigma^0_{meas})^2 \cdot \left(\frac{\partial V}{\partial \sigma^0_{meas}}\right)^2 + (\delta\sigma^0_{gr})^2 \cdot \left(\frac{\partial V}{\partial \sigma^0_{gr}}\right)^2 + (\delta\sigma^0_{df})^2 \cdot \left(\frac{\partial V}{\partial \sigma^0_{df}}\right)^2 + \\ (\delta\beta)^2 \cdot \left(\frac{\partial V}{\partial \beta}\right)^2 + + (\delta\eta_{df})^2 \cdot \left(\frac{\partial V}{\partial \eta_{df}}\right)^2 + (\delta\alpha)^2 \cdot \left(\frac{\partial V}{\partial \alpha}\right)^2 + (\delta h_{df})^2 \cdot \left(\frac{\partial V}{\partial h_{df}}\right)^2\end{array}} \qquad (3\text{-}17)$$

As for BIOMASAR-C, the precision of the estimates of σ^0_{df} and σ^0_{gr} is estimated as the standard deviation of the histograms of backscatter observations in areas of low and high canopy density, since the histograms summarize the uncertainties associated with estimating the parameters due to spatially variable imaging conditions, uncompensated topographic effects, etc. (e.g., variable soil/canopy moisture).

Reported accuracies of height and canopy density estimates derived from ICESAT GLAS are used to determine the uncertainty associated with estimating h_{df} and η_{df}. Following the results in Los et al. (2012) and Simard et al. (2011), who validated GLAS-based height estimates at boreal, temperate, sub-tropical, and tropical forest sites, we assumed standard deviations for height estimates at the GLAS footprint level as between 4 m (boreal) and 10 m (tropics). While there are a large number of studies on the estimation of canopy cover and closely related variables, such as fractional cover, gap probability or transmittance from LiDAR, only a few have presented comprehensive validation. It is thus not possible to provide forest type-specific numbers for the error in the BIOMASAR-L retrieval associated with errors in the parameter η_{df}. As indicated by Garcia et al. (2012), the error of the canopy cover estimate from ICESAT GLAS may be of the order of 15 to 20%. We therefore assume a conservative global error of 20%. Note that the parameters h_{df} and η_{df} are estimated with the average

GLAS height and density across all footprints covering an ALOS-2 1° × 1° tile that cover dense forest according to Landsat. It is therefore assumed that the standard deviation for the two parameters reduces as the square root of the number of GLAS footprints used in the estimation.

The precision of the forest transmissivity coefficient β and the related two-way attenuation coefficient α are the most difficult to specify and it is only possible to provide a best guess for BIOMASAR-C. In the case of β, the associated standard deviation may be inferred from the relationship between the forest transmissivity, simulated with the aid of GLAS height and optical canopy density estimates, and GSV (see Figure 3-10). The results presented in Figure 3-10 suggest that the standard deviation increases with increasing β. The 95% error bounds of the estimate for β increased from +/-0.002 ha m^{-3} in the case of low values of β that are valid in boreal and subtropical dry forests to +/-0.007 ha m^{-3} for the highest values of β that are applied in the tropics. For the two-way attenuation coefficient α, we assume a standard deviation of 0.25 dB m^{-1}, which is roughly consistent with the range of values reported in the literature (Ulaby et al., 1990; Chauhan et al., 1991; Shinohara et al., 1992; Sheen et al., 1994; Kurum et al., 2009; Praks et al., 2012).
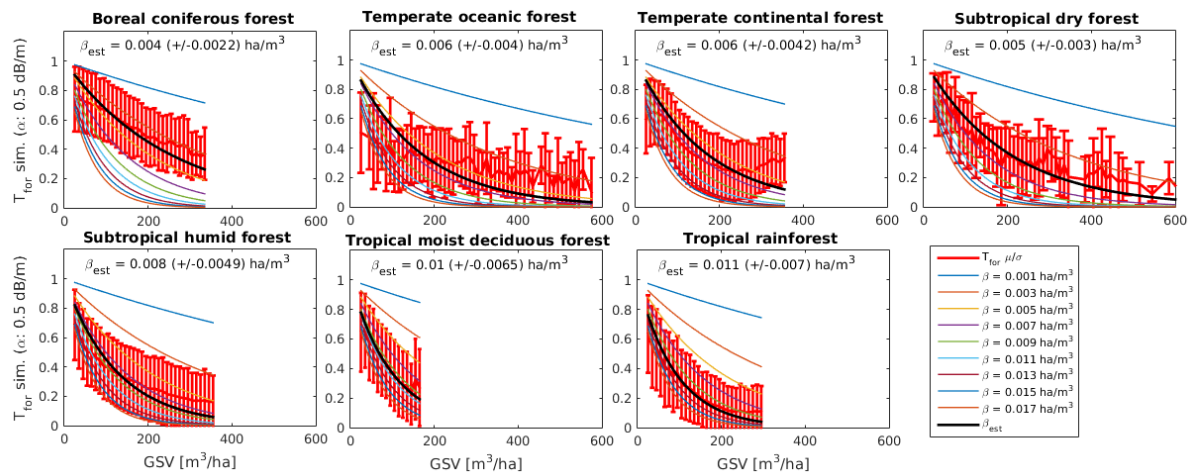

Figure 3-10: Estimates for β (incl. 95% confidence bounds) obtained for different FAO eco-regions. For details, refer to the ATBD of the GlobBiomass project [RD-8].

Equation (3-17) quantifies the standard deviation of GSV estimates derived from a single L-band observation, as in the case of BIOMASAR-L applied to one channel of the yearly JAXA L-band SAR backscatter mosaics (see [RD-5]). In a multi-temporal scenario (i.e., when multiple mosaics and/or Fine Beam Dual (FBD) and ScanSAR data are used (see [RD-5]), the standard deviation of the final GSV is obtained, similarly to the case of BIOMASAR-C, as a weighted multi-temporal combination of single image standard deviations and error covariance:

$$\delta(V_{mt})^2 = \sum_{i=1}^{N} w_i^2 \, \delta(V_i)^2 + 2 \sum_{i=1}^{N-1} \sum_{j=i+1}^{N} w_i \, w_j \, Cov(V_i, V_j) \qquad (3\text{-}18)$$

It the retrieval errors between single image GSV estimates are uncorrelated, the second term in Equation (3-18) becomes zero. Figure 3-11 shows the standard deviation for the BIOMASAR-L data product of GSV from ALOS-2 PALSAR-2 data assuming uncorrelated errors. For the map of GSV obtained with the BIOMASAR-L algorithm, refer to the ATBD of this project [RD-5].
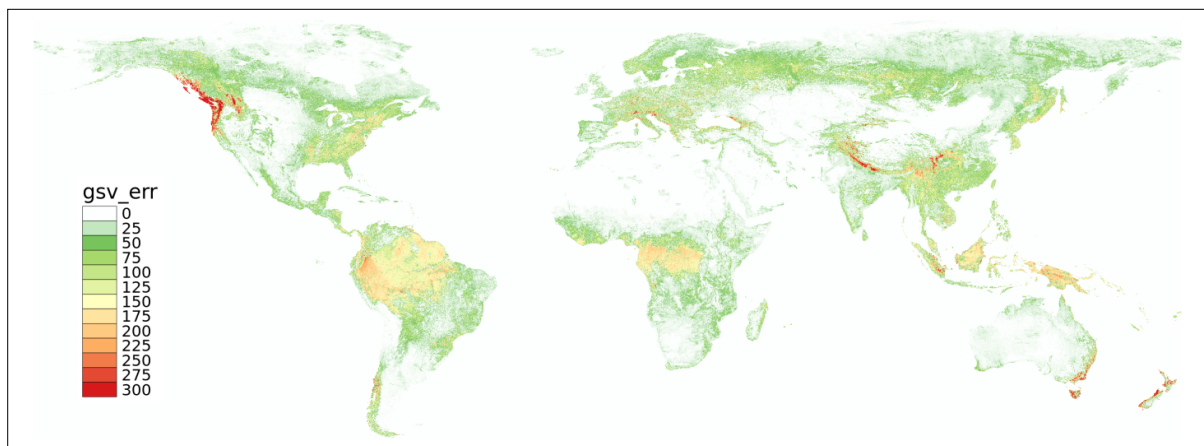
Figure 3-11: Standard deviation of BIOMASAR-L estimates of GSV assuming uncorrelated errors (i.e., first term of Equation (3-18)).

In practice, uncorrelated errors are unlikely, especially at low frequencies when the signal presents seasonal fluctuations and only minor date-to-date variability due to specific environmental conditions at the time of image acquisition.

In order to characterize the error correlation, we tested the use of airborne laser scanner (ALS) derived estimates of GSV/AGB as reference. For the AGB reported using laser-based maps, AGB was converted to GSV using the global database of BCEF estimates compiled in the frame of the GlobBiomass project [RD-8].

Figure 3-12 exemplifies the error correlation for a tropical forest site in Lope, Gabon, and a boreal forest site in Krycklan, Sweden. The laser-based maps of biomass used as reference were produced in the context of ESA's airborne radar campaigns AfriSAR and Biosar-2. In Lope, where FBD as well as ScanSAR data could be used to retrieve GSV, the error correlation was consistently around 0.5 to 0.6. Similar results were observed for other forest sites in the tropics. In Krycklan, instead, where only the three ALOS-2 PALSAR-2 FBD mosaics from 2015, 2016, and 2017 were available and only the HV-polarized backscatter was used to retrieve GSV, the error correlation was close to zero. With a negligible covariance term and only three estimates to combine, the multi-temporal combination for areas where only FBD data are available hardly improves the standard deviation of the estimates.
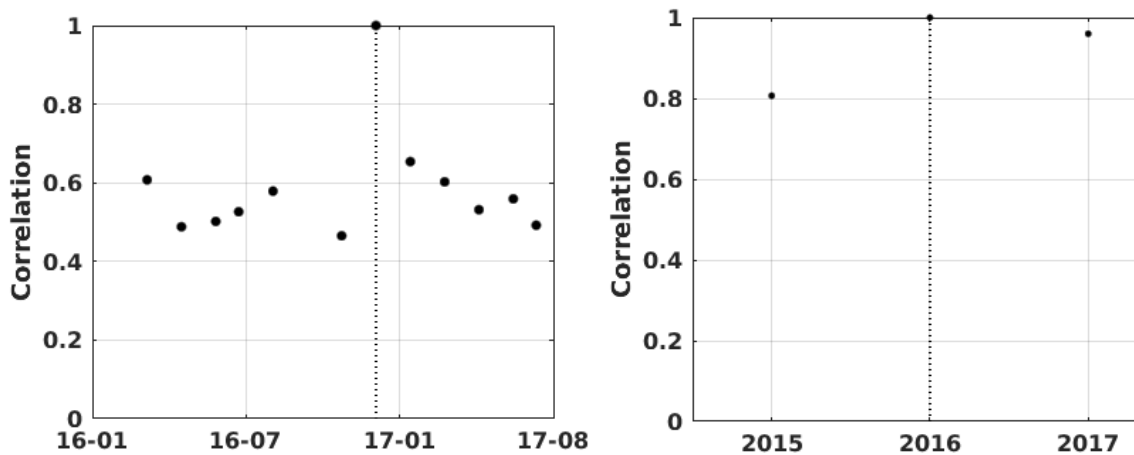
Figure 3-12: Correlation of GSV retrieval errors for a multi-temporal stack of L-band images acquired over Lope, Gabon (left) and Krycklan, Sweden (right). The vertical line denotes the reference image against which the correlation of retrieval errors with respect to the other available images was assessed.

The results obtained so far are considered to be a consequence of the fact that, over continuous tropical forest, the sensitivity of L-band backscatter to AGB is low, so that different temporally uncorrelated noise sources in the measurements (thermal noise, speckle, quantization noise, etc.) have a more pronounced effect on the retrievals than in areas where the sensitivity to AGB is higher. In addition, it should be noted that the FBD mosaics were compiled with a preference for images acquired under dry summer conditions whereas the ScanSAR dataset comprises multi-seasonal observations (i.e., the measurements reflect a wider range of imaging conditions). As for BIOMASAR-C, further investigations are required to assess the representativeness of these results across different forest ecosystems. However, some simplifying assumptions will be needed to characterize the error correlation matrix because of the unavailability of a global reference dataset.

3.3.3 BIOMASAR for AGB retrieval

As in the case of C-band (Section 3.2.3), the precision of AGB estimates derived from single L-band backscatter observations is quantified by propagating the standard deviations of backscatter measurements, σ^0_{meas}, estimates for the model parameters σ^0_{gr} and σ^0_{veg}, the coefficient relating canopy density and RH100, q, and the coefficients of the allometry relating canopy height and AGB, p_1 and p_2. The individual errors are determined in the same way as for C-band. However, in contrast to C-band, the modelling of L-band backscatter as function of canopy density necessitates the use of the full model in Eq. (3-1), which considers that the two-way tree transmissivity and hence the tree height and signal attenuation are not negligible at L-band [RD-5]. In the error propagation, we therefore have to propagate errors associated with the two-way signal attenuation coefficient. So far only very few measurements of the attenuation have been published. We here assume a standard deviation of 0.25 dB/m, which is roughly consistent with the range of values reported in the literature (Ulaby et al., 1990; Chauhan et al., 1991; Shinohara et al., 1992; Sheen et al., 1994; Kurum et al., 2009; Praks et al., 2012).

The standard deviation of multi-temporal AGB estimates is then quantified based on Eqs. 3-15 and 3-16. The error correlations between individual AGB estimates is assumed similar to those observed in the case of GSV (Figure 3-12)

3.4 Quantifying the precision of the merged biomass estimates

When combining estimates from BIOMASAR-C and BIOMASAR-L, Equation (3-19) can be used to calculate the standard deviation of the merged product starting from the standard deviations of the BIOMASAR-C and BIOMASAR-L estimates.

$$\delta(GSV)^2 = w^2(L)\delta(V_{mt,L})^2 + w^2(C)\delta(V_{mt,C})^2 \tag{3-19}$$

The equation is written in terms of GSV but applies equally to AGB.

3.5 Quantifying the precision of the conversion from GSV to AGB

In the GlobBiomass project, a global raster of the Biomass Conversion and Expansion Factors (BCEF) was obtained by producing two independent raster datasets of wood density (WD) and total-to-stem biomass ratio (BEF). Each data layer was generated from extensive in situ databases in cooperation with the Max Planck Institute for Biogeochemistry (MPI-BGC). In the first year of the CCI Biomass project, the GlobBiomass datasets of wood density and biomass expansion are used; refer to the ATBD of the GlobBiomass project [RD-8] for details on how these and the corresponding precision were derived.

When AGB is obtained by converting an estimate of GSV to AGB with a BCEF, the precision of the AGB estimates is obtained as:

$$\delta AGB = \sqrt{\left(\frac{\partial AGB}{\partial WD}\right)^2 \cdot \delta WD^2 + \left(\frac{\partial AGB}{\partial BEF}\right)^2 \cdot \delta BEF^2 + \left(\frac{\partial AGB}{\partial GSV}\right)^2 \cdot \delta GSV^2} \tag{3-20}$$

where δWD and δBEF represent the precision of the wood density and BEF terms respectively, and δGSV represents the precision of the merged GSV dataset. The partial derivatives of Equation (3-13) are reported in Annex B.

4 Methods to assign accuracies to AGB change estimates

AGB change is defined as the difference of AGB estimated at two epochs. In the ATBD [RD-5], we described the reasoning behind this definition and the implications concerning the reliability of the AGB changes based on estimates of AGB from different EO datasets. At the full resolution of the AGB maps, the variance of the AGB change $\delta(AGB_{change})^2$ is defined as the sum in quadrature of the individual variances $\delta(AGB_i)^2$ with i = 1 and 2 being the epoch of the AGB estimate.

$$\delta(AGB_{change})^2 = \delta(AGB_1)^2 + \delta(AGB_2)^2 \tag{3-21}$$

Additional terms will appear if a bias correction is applied to each of the AGB estimates. These terms correspond to the standard deviation of the bias estimate for date 1 and date 2. These terms, however, would be applied only at the spatial resolution of the bias maps, i.e., 0.1°, in which case the standard deviation of the two AGB estimates would need to account for the averaging and the spatial correlation of errors (Yang et al., 2020).

ANNEX A

Partial derivatives of Equation (3-12)

$$\left(\frac{\partial V}{\partial \sigma^0_{meas}}\right)_{\sigma^0_{gr},\sigma^0_{df},\beta,V_{df}} = \frac{e^{-\beta V_{df}}-1}{\beta\left[\left(\sigma^0_{meas}-\sigma^0_{gr}\right)e^{-\beta V_{df}}-\sigma^0_{meas}+\sigma^0_{df}\right]} \tag{S1}$$

$$\left(\frac{\partial V}{\partial \sigma^0_{gr}}\right)_{\sigma^0_{meas},\sigma^0_{df},\beta,V_{df}} = \frac{1}{\beta}\left[\frac{1}{\sigma^0_{df}-\sigma^0_{gr}}-\frac{e^{-\beta V_{df}}}{\left(\sigma^0_{meas}-\sigma^0_{gr}\right)e^{-\beta V_{df}}-\sigma^0_{meas}+\sigma^0_{df}}\right] \tag{S2}$$

$$\left(\frac{\partial V}{\partial \sigma^0_{df}}\right)_{\sigma^0_{meas},\sigma^0_{gr},\beta,V_{df}} = \frac{1}{\beta}\left[\frac{e^{-\beta V_{df}}}{\left(\sigma^0_{meas}-\sigma^0_{gr}\right)e^{-\beta V_{df}}-\sigma^0_{meas}+\sigma^0_{df}}-\frac{1}{\sigma^0_{df}-\sigma^0_{gr}}\right] \tag{S3}$$

$$\left(\frac{\partial V}{\partial \beta}\right)_{\sigma^0_{meas},\sigma^0_{gr},\sigma^0_{df},V_{df}} = \left\{\frac{\ln\left[\left(\sigma^0_{meas}-\sigma^0_{gr}\right)e^{-\beta V_{df}}-\sigma^0_{meas}+\sigma^0_{df}\right]-\ln\left(\sigma^0_{df}-\sigma^0_{gr}\right)}{\beta^2}+\frac{\left(\sigma^0_{meas}-\sigma^0_{gr}\right)V_{df}e^{-\beta V_{df}}}{\beta\left[\left(\sigma^0_{meas}-\sigma^0_{gr}\right)e^{-\beta V_{df}}-\sigma^0_{meas}+\sigma^0_{df}\right]}\right\} \tag{S4}$$

$$\left(\frac{\partial V}{\partial V_{df}}\right)_{\sigma^0_{meas},\sigma^0_{gr},\sigma^0_{df},\beta} = \frac{\left(\sigma^0_{meas}-\sigma^0_{gr}\right)e^{-\beta V_{df}}}{\left(\sigma^0_{meas}-\sigma^0_{gr}\right)e^{-\beta V_{df}}-\sigma^0_{meas}+\sigma^0_{df}} \tag{S5}$$

ANNEX B

Partial derivatives of Equation (3-20)

$$\left(\frac{\partial AGB}{\partial WD}\right)_{BEF,GSV} = BEF \cdot GSV \qquad \text{(S6)}$$

$$\left(\frac{\partial AGB}{\partial BEF}\right)_{WD,GSV} = WD \cdot GSV \qquad \text{(S7)}$$

$$\left(\frac{\partial AGB}{\partial GSV}\right)_{WD,BEF} = WD \cdot BEF \qquad \text{(S8)}$$

5 References

Breiman, L. (2001). Random Forests. *Machine Learning,* 45, 5-32.

Chauhan, N. S., Lang, R. H. and Ranson, K. J. (1991). Radar modeling of a boreal forest. *IEEE Transactions on Geoscience and Remote Sensing,* 29 (4), 627-638.

Garcia, M., Popescu, S., Riano, D., Zhao, K., Neuenschwander, A., Agca, M. and Chuvieco, E. (2012). Characterization of canopy fuels using ICESAT/GLAS data. *Remote Sensing of Environment,* 123, 81-89.

Kurum, M., Lang, R. H., O'Neill, P. E., Joseph, A. T., Jackson, T. J. and Cosh, M. H. (2009). L-Band radar estimation of forest attenuation for active/passive soil moisture inversion. *IEEE Transactions on Geoscience and Remote Sensing,* 47 (9), 3026-3040.

Los, S. O., Rosette, J., Kljun, N., North, P. R. J., Chasmer, L., Suárez, J. C., Hopkinson, C., Hill, R. A., van Gorsel, E., Mahoney, C. and Berni, J. A. J. (2012). Vegetation height and cover fraction between 60° S and 60° N from ICESat GLAS data. *Geoscientific Model Development,* 5, 413-432.

Nilsson, M., Nordkvist, K., Jonzén, J., Lindgren, N., Axensten, P., Wallerman, J., Egberth, M., Larsson, S., Nilsson, L., Eriksson, J. and Olsson, H. (2017). A nationwide forest attribute map of Sweden predicted using airborne laser scanning data and field data from the National Forest Inventory. *Remote Sensing of Environment,* 194, 447-454.

Praks, J., Antropov, O. and Hallikainen, M. (2012). LIDAR-aided SAR interferometry studies in boreal forest: Scattering phase center and extinction coefficient at X- and L-band. *Remote Sensing,* 50 (10), 3831-3843.

Santoro, M., Cartus, O., Carvalhais, N., Rozendaal, D., Avitabilie, V., Araza, A., de Bruin, S., Herold, M., Quegan, S., Rodríguez Veiga, P., Balzter, H., Carreiras, J., Schepaschenko, D., Korets, M., Shimada, M., Itoh, T., Moreno Martínez, Á., Cavlovic, J., Cazzolla Gatti, R., da Conceição Bispo, P., Dewnath, N., Labrière, N., Liang, J., Lindsell, J., Mitchard, E.T.A., Morel, A., Pacheco Pascagaza, A.M., Ryan, C.M., Slik, F., Vaglio Laurin, G., Verbeeck, H., Wijaya, A., Willcock, S., 2020. The global forest above-ground biomass pool for 2010 estimatedfrom high-resolution satellite observations (preprint). Earth System Science Data Discussions, https://doi.org/10.5194/essd-2020-148

Sheen, D. R., Malinas, N. P., Kletzli, D. W., Lewis, T. B. and Roman, J. F. (1994). Foliage transmission measurements using a ground-based ultrawide band (300-1300 MHz) SAR system. *IEEE Transactions on Geoscience and Remote Sensing,* 32 (1), 118-130.

Shinohara, H., Homma, T., Nohmi, H., Hirosawa, H. and Tagawa, T. (1992). Relation between L-band microwave penetration / backscattering characteristics and state of trees. In: *IGARSS'92*. City: IEEE Publications, Piscataway, NJ, 539-541.

Simard, M., Pinto, N., Fisher, J. B. and Baccini, A. (2011). Mapping forest canopy height globally with spaceborne lidar. *Journal of Geophysical Research - Biogeosciences,* 116, G04021.

Ulaby, F. T., Whitt, M. W. and Dobson, M. C. (1990). Measuring the propagation properties of a forest canopy using a polarimetric scatterometer. *IEEE Transactions on Antennas and Propagation,* 38 (2), 251-258.

Yang, H., Ciais, P., Santoro, M., Huang, Y., Li, W., Wang, Y., Bastos, A., Goll, D., Arneth, A., Anthoni, P., Arora, V.K., Friedlingstein, P., Harverd, V., Joetzjer, E., Kautz, M., Lienert, S., Nabel, J.E.M.S., O'Sullivan, M., Sitch, S., Vuichard, N., Wiltshire, A., Zhu, D., (2020). Comparison of forest above-ground biomass from dynamic global vegetation models with spatially explicit remotely sensed observation-based estimates. *Global Change Biology*, 26, 3997–4012. https://doi.org/10.1111/gcb.15117